Exploring the optical behaviour of a Type Iax supernova SN 2014dt

Mridweeka Singh,[1,2]⋆ Kuntal Misra,[1]⋆ D. K. Sahu,[3]⋆ Raya Dastidar,[1,4]
Anjasha Gangopadhyay,[1,2] Subhash Bose,[5] Shubham Srivastav,[3] G. C. Anupama,[3]
N. K. Chakradhari,[2] Brajesh Kumar,[3] Brijesh Kumar[1] and S. B. Pandey[1]

[1]*Aryabhatta Research Institute of observational sciencES (ARIES), Manora Peak, Nainital 263 001, India*
[2]*School of Studies in Physics and Astrophysics, Pandit Ravishankar Shukla University, Chattisgarh 492 010, India*
[3]*Indian Institute of Astrophysics, Koramangala, Bangalore 560 034, India*
[4]*Department of Physics and Astrophysics, University of Delhi, Delhi 110 007, India*
[5]*Kavli Institute for Astronomy and Astrophysics, Peking University, 5 Yiheyuan Road, Haidian District, Beijing 100871, China*

ABSTRACT

We present optical photometric (up to ∼410 d since B_{max}) and spectroscopic (up to ∼157 d since B_{max}) observations of a Type Iax supernova (SN) 2014dt located in M61. SN 2014dt is one of the brightest and closest ($D \sim 20$ Mpc) discovered Type Iax SN. It best matches the light-curve evolution of SN 2005hk and reaches a peak magnitude of $M_B \sim -18.13 \pm 0.04$ mag with $\Delta m_{15} \sim 1.35 \pm 0.06$ mag. The early spectra of SN 2014dt are similar to other Type Iax SNe, whereas the nebular spectrum at 157 d is dominated by narrow emission features with less blending as compared to SNe 2008ge and 2012Z. The ejecta velocities are between 5000 and 1000 km s^{-1}, which also confirms the low-energy budget of Type Iax SN 2014dt compared to normal Type Ia SNe. Using the peak bolometric luminosity of SN 2005hk, we estimate the ^{56}Ni mass of ∼0.14 M$_\odot$. The striking similarity between SN 2014dt and SN 2005hk implies that a comparable amount of ^{56}Ni would have been synthesized in the explosion of SN 2014dt.

Key words: techniques: photometric – techniques: spectroscopic – supernovae: general – supernovae: individual: SN 2014dt – galaxies: individual: M61.

1 INTRODUCTION

The last two decades have witnessed the advent of a new subclass of Type Ia supernovae (SNe) that are grouped together and these are commonly known as Type Iax SNe (Foley et al. 2013). The rate of occurrence of Type Iax SNe is 31^{+19}_{-13} for every hundred normal Type Ia SNe (Foley et al. 2013). Type Iax SNe exhibit distinct properties both photometrically and spectroscopically when compared to the normal Type Ia SNe. The secondary peak in the near-infrared (NIR) light curves of Type Ia SNe is not seen in the NIR light curves of Type Iax SNe (Li et al. 2003). A wide range is seen in the peak absolute brightness ($M_V = -14$ to -18 mag). Their expansion velocities are (∼4000 to ∼9000 km s^{-1}) half of that of Type Ia SNe (∼10,000 to ∼15,000 km s^{-1}). For a small sample of objects similar to SN 2002cx, McClelland et al. (2010) suggested that there were correlations between the peak luminosity, light-curve shape and ejecta velocity. Narayan et al. (2011) also derived scaling relations between ejecta velocity and decline rate using the Arnett formulation. Narayan et al. (2011) found that the ejecta mass

of Type Iax SNe was between 1 and 1.4 M$_\odot$ (with SN 2008ha being an exception). With a slightly larger sample, the ejecta mass of Type Iax SNe was estimated to be 0.5 ± 0.2 M$_\odot$ (Foley et al. 2013). With a greater number of Type Iax SNe discovered, correlations between the decline rate and ejecta velocity and between the peak luminosity and decline rate were found by Foley et al. (2013) and Magee et al. (2016). These are subluminous events but their early time spectra are similar to SN 1991T-like over-luminous events. Often their maximum light spectra show signs of unburned carbon, ∼82 per cent of Type Iax SNe have clear absorption of carbon whereas only 30 per cent of Type Ia SNe have carbon in their pre-maximum spectra (Foley et al. 2013). The nebular spectra of Type Ia SNe are associated with the forbidden emission lines of iron group elements, whereas Type Iax SNe have permitted lines of these iron group elements along with intermediate-mass elements (S, Ca, etc.). It is also seen that the late-time spectra of Type Iax SNe have calcium interior to iron (Foley et al. 2013), which is the opposite of what we see in Type Ia SNe. The two-component model proposed by Foley et al. (2016) discusses the origin of broad emission lines from the ejecta and narrow forbidden lines originating from a wind that is thought to be associated with the remnant of the progenitor.

The progenitors are a very good source for a clear distinction between various subclasses of Type Ia SNe. Liu et al. (2015b) proposed

different explosion scenarios and progenitor systems to investigate the nature of these events. It is widely accepted that a thermonuclear explosion of a carbon oxygen white dwarf (Chandrasekhar or sub-Chandrasekhar mass limit of a white dwarf) gives rise to the peculiar Type Iax SNe (Foley et al. 2009; Jordan et al. 2012; Kromer et al. 2013, 2015; Fink et al. 2014; Stritzinger et al. 2015; Liu et al. 2015a). However, one of the Type Iax SNe, SN 2008ha, supports the core-collapse scenario with the progenitor being a hydrogen-deficient massive star that has a main-sequence mass of 13 $M_\odot$ (Valenti et al. 2009; Moriya et al. 2010). Foley et al. (2009, 2010b) presented the maximum light spectrum of SN 2008ha with the association of C/O burning features, which contradicts the core-collapse origin. One of the most important differences between Type Ia and Type Iax SNe is that there is no direct observational evidence of a progenitor system of Type Ia SNe yet. In contrast, probable progenitors are imaged for Type Iax SNe. In the case of SN 2012Z, a coincident luminous blue source at the location of the SN was detected in the pre-explosion *Hubble Space Telescope* (*HST*) images (McCully et al. 2014a). Two other SNe with pre-explosion images are SNe 2008ge and 2014dt (for details, see Foley et al. 2010a, 2015). SNe 2004cs and 2007J are two special cases in which the classification is in question. They were classified as both Type IIb and Iax, showing He features by several authors (for details, see Rajala et al. 2005; Lee et al. 2007; Filippenko et al. 2007a,b; Foley et al. 2009, 2013; White et al. 2015). The claim of a helium connection with the rare Type Iax SNe and hence their progenitors is questionable, which is solely based on two objects (White et al. 2015).

In this paper, we examine the photometric and spectroscopic properties of a peculiar Type Iax SN 2014dt. In Section 3, we describe the data acquisition and reduction procedure. In Section 4, we discuss the distance estimates and extinction of the host galaxy. The estimated magnitudes are used to construct and study the multiband light curves in Section 5, where we also discuss the absolute magnitude, colour evolution and pseudo-bolometric light curves of SN 2014dt along with other Type Iax SNe. In Section 6, we give a detailed description of the spectral evolution and spectral modelling. In Section 7, we summarize the results obtained.

2 SN 2014DT

SN 2014dt was discovered on 2014 October 29.838 UT (JD = 245 6960.338) in an unfiltered CCD frame with a 0.50-m *f*/6.8 reflector telescope at Takanezawa, Tochigi-kenn in the galaxy M61 (Nakano et al. 2014). On October 30.50 UT, the SN was 13.6 mag bright in the *V* filter. SN 2014dt is one of the brightest (peak magnitude ∼13.6 in the *V* filter) and closest discovered Type Iax SNe (*D* ∼ 20 Mpc). The SN is 33.9 arcsec east and 7.2 arcsec south of the centre of the host galaxy M61, which has hosted six other Type II SNe. Spectroscopic observations of SN 2014dt with the 182-cm Copernico Telescope on October 31.20 UT showed characteristics of a peculiar Type Ia SN with a relatively blue continuum, weak Si II absorption at 6350 Å and Fe II lines at 4300 and 5000 Å (Ochner et al. 2014) similar to SN 2002cx at +17 d, which means that it is classified as a Type Iax SN. Along with SNe 2008ge and 2012Z, SN 2014dt is the third member of the Type Iax class with available pre-explosion images. Based on the pre-explosion images, Foley et al. (2015) suggested that the progenitor of SN 2014dt could be a carbon oxygen white dwarf plus helium star system with a hotter donor. They suggest that the progenitor system of SN 2014dt might have a low-mass red giant or a main-sequence star as a companion (more details are given in

Table 1. Details of SN 2014dt and its host galaxy M61. The host galaxy parameters are taken from the NED.

Host galaxy, M61	
Galaxy type	SAB(rs)bc
Constellation	Virgo
Redshift	0.005224 ± 0.000007
Major diameter	6.5 arcmin
Minor diameter	5.8 arcmin
Heliocentric radial velocity	1566 ± 2 km s^{-1}
SN 2104dt	
RA (J2000.0)	$12^h21^m57{.}^s57$
Dec. (J2000.0)	$+04^d28^m18{.}^s5$
Luminosity distance	21.44 ± 0.03 Mpc
Galactic extinction $E(B-V)$	0.02 mag
SN Type	Iax
Offset from nucleus	33.9 E,7.2 S arcsec
Date of discovery	245 6960.338 (JD)

Section 6). The details of the host galaxy M61 and SN 2014dt are given in Table 1.

3 DATA ACQUISITION AND REDUCTION

3.1 Optical photometric observations

A rigorous follow-up campaign of SN 2014dt started immediately after the discovery with the 104-cm Sampurnanand Telescope (ST; Sagar 1999), the 130-cm Devasthal Fast Optical Telescope (DFOT; Sagar et al. 2012) situated at the Aryabhatta Research Institute of observational sciencES (ARIES), Nainital, India, and the 201-cm Himalayan Chandra Telescope (HCT; see Prabhu & Anupama 2010 and references therein) situated at the Indian Astronomical Observatory (IAO), Hanle, India. The details of the detectors used with different telescopes are given in Table 2. The photometric observations of SN 2014dt started ∼1 d after discovery and lasted up to ∼400 d. Along with the SN field, bias frames for removing zero integration noise and flat frames for removing non-uniformity of pixel-to-pixel response were also taken. The science frames were corrected for bias and flat-fields by using the packages available in IRAF.[1] Cosmic rays were removed by using the task L.A. Cosmic (van Dokkum 2001). To improve the signal-to-noise ratio (S/N), wherever multiple frames were available on a single night, images were co-added. Because the SN is situated away from the galaxy centre, near one of the spiral arms of the galaxy and lies in a relatively clean part of the galaxy, we did not perform template subtraction to remove the galaxy contribution. We performed point spread function (PSF) photometry using packages in DAOPHOT II (Stetson 1987) to estimate the SN magnitudes. We took the first aperture equal to the mean FWHM of the frame, and the inner sky annulus was taken to be four times the FWHM. An eight-pixel wide-sky annulus was selected with respect to the inner-sky annulus.

To convert the instrumental magnitudes into standard magnitudes, we observed the Landolt equatorial standards (Landolt 2009) on 2014 November 24 and 2015 December 01, along with the SN field in the *VRI* and *UBVRI* bands, respectively. These

---

[1] IRAF stands for Image Reduction and Analysis Facility, which is distributed by the National Optical Astronomy Observatories, operated by the Association of Universities for research in Astronomy, Inc., under cooperative agreement with the National Science Foundation.

Table 2. Details of instruments and detectors.

Telescope	Detector	Area (arcmin^2)	Pixel size (μm)	Plate scale (arcsec pixel^{-1})	Readout noise (e$^-$)	Gain (e$^-$ ADU^{-1})
ST	2k×2k	13.5×13.5	24	0.37	5.3	10.00
ST	1k×1k	6.5×6.5	24	0.37	7.0	11.98
DFOT	2k×2k	18.0×18.0	13.5	0.54	7.0	2.0
HCT	2k×4k	10.0×10.0	15	0.17	4.8	1.22

Table 3. Star ID along with magnitude of secondary standard stars used for calibration.

Star ID	RA (h:m:s)	Dec. (d:m:s)	B (mag)	V (mag)	R (mag)	I (mag)
A	12:22:07.92	+04:33:04.5	16.984 ± 0.028	16.728 ± 0.011	16.411 ± 0.010	16.135 ± 0.011
B	12:22:04.10	+04:32:29.5	15.997 ± 0.027	15.438 ± 0.011	14.971 ± 0.009	14.606 ± 0.008
C	12:22:06.00	+04:30:52.1	17.943 ± 0.031	17.579 ± 0.017	17.246 ± 0.010	16.976 ± 0.017
D	12:22:02.37	+04:30:08.6	19.089 ± 0.051	17.944 ± 0.013	17.023 ± 0.010	16.212 ± 0.014
E	12:22:06.08	+04:28:41.4	18.419 ± 0.036	17.429 ± 0.012	16.650 ± 0.010	16.024 ± 0.010
F	12:22:02.96	+04:24:52.2	17.923 ± 0.031	16.910 ± 0.011	16.105 ± 0.009	15.481 ± 0.009
G	12:22:06.76	+04:23:23.5	17.916 ± 0.031	16.841 ± 0.011	16.046 ± 0.009	15.404 ± 0.009
H	12:21:56.37	+04:23:49.3	15.090 ± 0.027	14.647 ± 0.011	14.271 ± 0.009	13.951 ± 0.008
I	12:21:44.94	+04:23:46.0	17.309 ± 0.029	16.724 ± 0.011	16.221 ± 0.009	15.815 ± 0.010
J	12:21:43.86	+04:24:23.3	17.596 ± 0.030	17.235 ± 0.012	16.894 ± 0.010	16.618 ± 0.011
K	12:21:44.50	+04:25:23.9	17.771 ± 0.030	17.488 ± 0.012	17.174 ± 0.011	16.876 ± 0.014
L	12:21:48.98	+04:26:20.8	14.237 ± 0.027	13.872 ± 0.011	13.529 ± 0.009	13.324 ± 0.011
M	12:21:40.25	+04:28:17.4	18.915 ± 0.044	16.924 ± 0.012	16.635 ± 0.013	14.993 ± 0.009
N	12:21:39.45	+04:29:04.8	17.555 ± 0.029	17.095 ± 0.012	16.660 ± 0.010	16.283 ± 0.010
O	12:21:37.95	+04:30:26.5	17.482 ± 0.029	17.211 ± 0.014	16.804 ± 0.013	16.272 ± 0.020
P	12:21:48.24	+04:32:26.0	17.025 ± 0.028	15.898 ± 0.011	14.967 ± 0.009	14.087 ± 0.008
Q	12:21:52.85	+04:30:25.9	16.344 ± 0.027	15.456 ± 0.011	14.768 ± 0.009	14.166 ± 0.008

observations were carried out under good photometric conditions (seeing in the *V* band was ∼1.7 arcsec). We selected stars associated with PG 0231, PG 0918, PG 0942, PG 2213, PG 2331, SA 92 and SA 95 fields for observations. Their brightness range varied in the range $16.28 < V < 12.27$ and the colour range was $-0.32 < B - V < 1.45$ mag. The standard fields were observed at different airmasses ranging between 1.9 and 1.3 on 2015 December 01. We used the standard magnitudes and the instrumental magnitudes of the Landolt field stars to simultaneously fit for the extinction coefficient, colour coefficient and zero-point following the least-squares regression technique described in Stetson (1992). However, Landolt standards on 2014 November 24 were observed only for estimating the zero-points; we used site extinction values (Stalin et al. 2008) to apply the extinction correction while extinction values were derived for the data acquired on 2015 December 01.

The fitted values of these coefficients were used to transform the instrumental magnitudes of the standard stars to standard magnitudes. The root-mean-square (rms) scatter between transformed and standard magnitude of Landolt stars was found to be ∼0.04 mag in the *B* band, ∼0.02 mag in the *V* band, ∼0.02 mag in the *R* band and ∼0.03 mag in the *I* band. Using these transformation equations, we generated 17 local standards in the SN field, which were non-variables. The final magnitudes (weighted average for two sets of observations for *VRI* bands) of these 17 local standards are listed in Table 3 and marked in Fig. 1 along with the SN location. For all other nights, zero-points were determined and SN magnitudes were calibrated differentially using these local standards. The errors due to calibration and photometry were added in quadrature to estimate the final error in SN magnitudes. The calibrated SN magnitudes and the associated errors in *BVRI* filters are listed in Table 4.
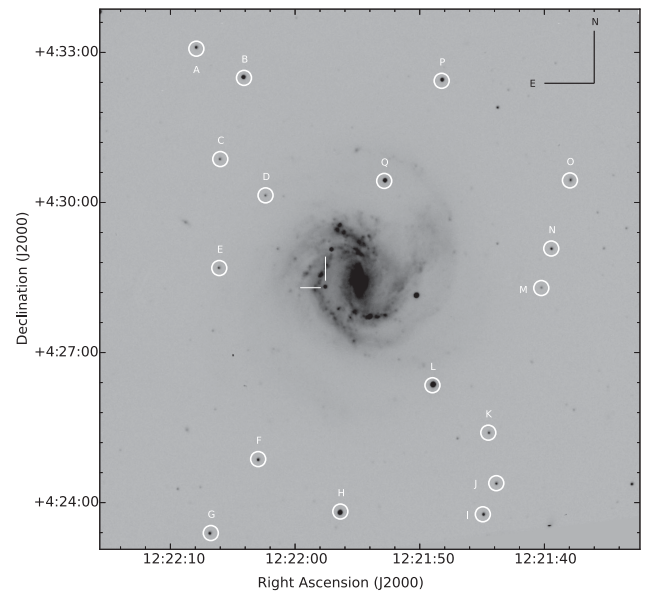
Figure 1. SN 2014dt in M61 (the star IDs for local standards have been marked). This image was taken on 2015 January 20 in the *V* band from the 104-cm ST, which covers an area of about 13.5×13.5 arcmin^2.

3.2 Optical spectroscopic observations

Long-slit low-resolution spectroscopic data at 18 epochs were obtained with the HCT, equipped with the Hanle Faint Object Spectrograph and Camera (HFOSC). To cover the entire optical region, a pair of grisms, Gr7 (3800–7800 Å) with a resolution of 1330

Table 4. Log of optical observations. Phase has been calculated with respect to $B_{max} = 245\ 6950.34$.

Date	Phase (d)	B (mag)	V (mag)	R (mag)	I (mag)	Telescope
2014/10/30	9.83	14.105 ± 0.015	13.620 ± 0.037	13.296 ± 0.020	13.255 ± 0.009	HCT
2014/11/23	33.17	16.186 ± 0.019	15.015 ± 0.017	14.610 ± 0.024	14.179 ± 0.012	HCT
2014/11/25	36.14	16.156 ± 0.015	15.039 ± 0.019	14.610 ± 0.023	–	DFOT
2014/11/26	37.12	16.161 ± 0.014	15.061 ± 0.019	14.626 ± 0.025	14.238 ± 0.013	DFOT
2014/12/01	42.11	16.338 ± 0.014	15.221 ± 0.016	14.940 ± 0.023	14.447 ± 0.011	HCT
2014/12/04	45.13	16.414 ± 0.015	15.336 ± 0.017	14.961 ± 0.023	14.556 ± 0.010	HCT
2014/12/05	46.38	16.196 ± 0.024	15.309 ± 0.019	14.973 ± 0.024	14.573 ± 0.017	ST
2014/12/08	49.15	16.418 ± 0.023	15.427 ± 0.018	15.059 ± 0.030	14.642 ± 0.024	HCT
2014/12/09	50.38	16.524 ± 0.025	–	15.069 ± 0.024	14.675 ± 0.015	ST
2014/12/10	51.33	16.462 ± 0.028	15.467 ± 0.021	15.090 ± 0.024	14.701 ± 0.017	ST
2014/12/16	57.38	–	15.618 ± 0.019	15.264 ± 0.024	14.876 ± 0.012	ST
2014/12/29	70.33	–	15.893 ± 0.028	15.651 ± 0.028	15.187 ± 0.016	ST
2015/01/04	76.32	–	16.095 ± 0.018	15.702 ± 0.025	–	ST
2015/01/06	78.39	–	16.216 ± 0.026	15.767 ± 0.027	15.336 ± 0.019	ST
2015/01/07	78.99	–	16.131 ± 0.022	15.773 ± 0.024	15.324 ± 0.017	HCT
2015/01/09	81.29	–	16.094 ± 0.020	15.800 ± 0.025	15.375 ± 0.013	ST
2015/01/20	92.29	–	16.303 ± 0.024	15.986 ± 0.028	15.556 ± 0.017	ST
2015/01/30	102.28	–	16.479 ± 0.023	16.153 ± 0.029	15.668 ± 0.021	ST
2015/02/04	107.36	17.489 ± 0.097	16.652 ± 0.035	16.226 ± 0.028	15.774 ± 0.022	ST
2015/04/06	168.17	–	17.313 ± 0.032	16.729 ± 0.028	16.189 ± 0.018	ST
2015/04/07	169.16	18.424 ± 0.061	17.296 ± 0.025	16.775 ± 0.031	16.233 ± 0.024	ST
2015/04/08	170.12	18.177 ± 0.053	17.257 ± 0.031	16.894 ± 0.029	16.272 ± 0.023	ST
2015/04/18	180.11	–	17.384 ± 0.032	16.855 ± 0.029	16.216 ± 0.028	ST
2015/04/21	183.12	–	17.412 ± 0.034	16.850 ± 0.032	16.216 ± 0.025	ST
2015/04/24	186.15	–	17.435 ± 0.030	16.859 ± 0.033	16.371 ± 0.029	ST
2015/05/02	194.13	–	17.638 ± 0.062	16.940 ± 0.039	16.370 ± 0.029	ST
2015/05/03	195.06	–	17.663 ± 0.049	17.100 ± 0.053	16.369 ± 0.023	ST
2015/05/05	197.14	–	17.520 ± 0.032	17.007 ± 0.031	16.189 ± 0.044	ST
2015/05/30	222.44	–	–	–	16.784 ± 0.023	ST
2015/12/01	407.06	–	19.024 ± 0.025	18.323 ± 0.026	17.643 ± 0.014	HCT

Table 5. Log of spectroscopic observations. Phase has been calculated with respect to $B_{max} = 245\ 6950.34$.

Date	Phase (d)	Grism	Spectral range (Å)	Telescope
2014/11/11	23.14	Gr07,Gr08	3800–6840, 5800–8350	HFOSC, HCT
2014/11/17	29.16	Gr07,Gr08	3800–6840, 5800–8350	HFOSC, HCT
2014/11/23	35.13	Gr07,Gr08	3800–6840, 5800-8350	HFOSC, HCT
2014/12/01	42.16	Gr07,Gr08	3800–6840, 5800–8350	HFOSC, HCT
2014/12/04	46.09	Gr07,Gr08	3800–6840, 5800–8350	HFOSC, HCT
2014/12/08	49.16	Gr07,Gr08	3800-6840, 5800–8350	HFOSC, HCT
2014/12/10	52.1	Gr07	3800–6840	HFOSC, HCT
2014/12/19	61.07	Gr07,Gr08	3800–6840, 5800–8350	HFOSC, HCT
2014/12/26	67.17	Gr07	3800–6840	HFOSC, HCT
2015/01/04	77.19	Gr07,Gr08	3800–6840, 5800–8350	HFOSC, HCT
2015/01/06	79	Gr07,Gr08	3800–6840, 5800–8350	HFOSC, HCT
2015/01/18	91.09	Gr07,Gr08	3800–6840, 5800–8350	HFOSC, HCT
2015/01/25	97.97	Gr07,Gr08	3800–6840, 5800–8350	HFOSC, HCT
2015/02/01	105.02	Gr07,Gr08	3800–6840, 5800–8350	HFOSC, HCT
2015/02/05	109.09	Gr07,Gr08	3800–6840, 5800–8350	HFOSC, HCT
2015/02/23	127.02	Gr07,Gr08	3800–6840, 5800–8350	HFOSC, HCT
2015/03/12	143.95	Gr07,Gr08	3800–6840, 5800–8350	HFOSC, HCT
2015/03/25	156.89	Gr07,Gr08	3800–6840, 5800–8350	HFOSC, HCT

and Gr8 (5800–9200 Å) with a resolution 2190, is used with the HFOSC for spectroscopic observations. The slit width (0.77 and 1.92 arcsec) was chosen so as to avoid contamination because of the host. Exposure time was varied between 600 and 1800 s in order to obtain good S/N spectra. For wavelength calibration, arc lamps (FeAr and FeNe) were observed just after SN exposure; for flux calibration, spectrophotometric standard stars (Feige 34, Feige 110 and HZ 44) were observed each night along with the SN. Necessary

pre-processing and spectral reduction were carried out with standard tasks in IRAF. To cross-check the wavelength calibration, O I emission lines at 5577, 6300 and 6364 Å were used and, in some cases, a wavelength shift within 0.2–4 Å was found. This shift was applied to correct the spectrum. The blue and red region spectra in Gr7 and Gr8 were combined by applying a scaling factor to obtain the final spectrum on a relative flux scale. The relative flux spectra were brought to an absolute flux scale by estimating the scalefactors from *BVRI* magnitudes. The telluric lines were not removed from the spectra. Spectra were corrected for redshift using DOPCOR. The log of spectroscopic observations is given in Table 5.

4 DISTANCE AND EXTINCTION

Several distance measurements ranging between 7.59 Mpc (Bottinelli et al. 1984) and 35.50 ± 0.25 Mpc (Sparks 1994) are available in the NASA/IPAC Extragalactic Data base (NED) for the host galaxy of SN 2014dt. A weighted average of recent distance measurements with different methods – CO and H I (Schoeniger & Sofue 1997), SCM (Roy et al. 2011; Pejcha & Prieto 2015), EPM (Bose & Kumar 2014) and the photospheric magnitude method (Rodríguez, Clocchiatti & Hamuy 2014) – gives a value of 15.56 ± 0.15 Mpc. Foley et al. (2015) used a distance of 12.3 Mpc to put constraints on the progenitor of SN 2014dt. However, Fox et al. (2016) argue that absolute magnitudes of SN 2014dt are similar to absolute magnitudes of SNe 2005hk and 2012Z if a distance of 19.3 Mpc is adopted. Using the redshift $z = 0.005224 \pm 0.000007$ (Binggeli, Sandage & Tammann 1985), we estimate the luminosity distance of M61 to be 21.44 ± 0.03 Mpc for $H_0 = 73 \pm 5$ km s^{-1} Mpc^{-1}, $\Omega_m = 0.27$ and $\Omega_v = 0.73$. Because there is a range of distance measurements available, we adopt the luminosity distance for further analysis in the present work.

The galactic reddening in the direction of SN 2014dt is $E(B - V) = 0.02$ mag (Schlafly & Finkbeiner 2011). The blue continuum and absence of Na ID absorption lines in the spectrum of SN 2014dt hints at a negligible host galaxy reddening, which is also supported by the fact that SN 2014dt lies in a relatively clean part of the face-on spiral galaxy M61 (Foley et al. 2015). Fox et al. (2016) compared the colour evolution of SN 2014dt with SNe 2005hk and 2012Z (hosts of both of these SNe have low extinction) to constrain the low reddening in SN 2014dt. Therefore, we use only the galactic reddening value as the total reddening with $E(B - V) = 0.02$ mag and $R_v = 3.1$ in our work.

5 TEMPORAL EVOLUTION OF SN 2014DT

5.1 Prime light-curve features

Fig. 2 shows the light-curve evolution of SN 2014dt in the *BVRI* bands up to ~400 d after discovery. We started the observing campaign ~1 d after discovery. The SN was discovered post-peak, so therefore it is difficult to estimate the peak magnitude and the time of maximum. We adopt the template fitting method to estimate magnitudes at maximum in different bands and time of maximum using a χ^2 minimization technique which solves simultaneously for both peak magnitude and time of maximum. The template light curves are stretched in time and scaled in magnitudes to obtain the best match with the observed data set. We take SN 2005hk (Sahu et al. 2008; McCully et al. 2014b) and SN 2012Z (Yamanaka et al. 2015) as templates, which fall in the category of well-observed Type Iax SNe. We supplement our *B*- and *V*-band data of SN 2014dt with data published in Fox et al. (2016) to increase the sampling of our light
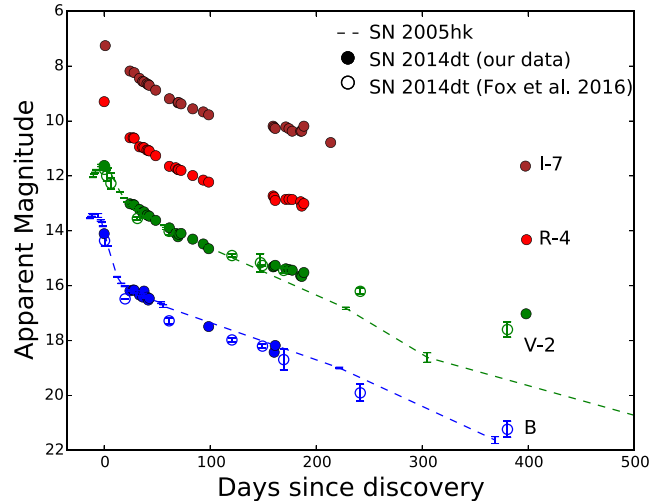

Figure 2. Broad-band *BVRI* light curves of SN 2014dt along with best-fitting templates of SN 2005hk in the *B* and *V* bands. We have supplemented the data from Fox et al. (2016) in the *B* and *V* bands. The light curves in different bands are shifted arbitrarily for clarity. The error bars are smaller than the point size.

curve. SN 2005hk provides the best match with SN 2014dt. The *B*- and *V*-band light curves of SN 2014dt with best-fitting templates of SN 2005hk are shown in Fig. 2. The best fit estimates the time of B_{max} to be JD = 245 6950.34. The results obtained by template fitting are listed in Table 6. Fox et al. (2016) also compared the multiwavelength light curve of SN 2014dt with SNe 2005hk and 2012Z and concluded that SN 2014dt peaked around 2014 October 20 (MJD = 245 6950). Using the spectra taken on 1.4 and 19.6 rest-frame days after discovery, Foley et al. (2016) find that SN 2014dt was discovered +4 ± 7 d since maximum and estimate B_{max} to be 2014 October 25 (JD = 245 6955.7). Our estimation of B_{max} (JD = 245 6950.34) is consistent with the values derived by Fox et al. (2016) and Foley et al. (2016). We use our estimate of B_{max} (JD = 245 6950.34) throughout this paper and consider this as the zero phase in time. Combining our *B*-band data and data taken from Fox et al. (2016), we estimate the luminosity decline rate Δm_{15} (i.e. the change in the magnitude of SN in the *B* band at maximum and after 15 d of maximum) for SN 2014dt to be 1.35 ± 0.06 mag, which is less than that obtained for SN 2005hk ($\Delta m_{15} = 1.68 \pm 0.05$ mag; Sahu et al. 2008).

Radioactive decay of ^{56}Ni to ^{56}Co is responsible for early time light curves of Type Ia SNe and the late-time light curves are powered by decay of ^{56}Co to ^{56}Fe. In the case of SN 2014dt, the light curves follow a linear decline up to 100 d, after which a flattening is noticed in the light curves. The decay rates in the *BVRI* bands between 34 and 108 d are 1.96 ± 0.07, 2.46 ± 0.03, 2.43 ± 0.03 and 2.14 ± 0.03 mag (100 d)$^{-1}$, respectively. The early time decay rates of SNe 2005hk and 2014dt are listed in Table 6. Up to 300 d, the light curves of normal Type Ia SNe are governed by the trapping of gamma rays after which the light curves transition to the regime governed by full trapping of positrons. Our optical light curves up to ~100 d are well within the gamma-ray regime. At very late epochs (298–326 d), a flattening is reported in the IR light curves of SN 2014dt by Fox et al. (2016). The unavailability of data points between ~200 and 400 d in our optical light curves does not allow us to make a similar comparison with the NIR light curves. In the case of SN 2014dt, we also estimate the late-time decay rates during the

Table 6. Parameters of SN 2014dt.

SN 2014dt	*B* band[a]	*V* band	*R* band	*I* band
Epoch of maximum	950.34	959.71	–	–
Magnitude at maximum (mag)	13.59 ± 0.04	13.39 ± 0.02	–	–
Absolute magnitude at maximum (mag)	−18.13 ± 0.04	−18.33 ± 0.02	–	–
Δm_{15} (mag)	1.35 ± 0.06	–	–	–
	Decline rate mag (100 d)$^{-1}$			
Time range (d)				
34–108	1.96 ± 0.07	2.46 ± 0.03	2.43 ± 0.03	2.14 ± 0.03
168–200	–	1.16 ± 0.18	0.82 ± 0.21	–
168–220	–	–	–	0.87 ± 0.22
	Decline rate mag (100 d)$^{-1}$			
SN 2005hk				
Time range (d)				
20–45	2.1	2.7	3.1	3.1
230–380	–	1.5	1.1	–

Note. [a]JD 245 3000+.

period 168–200 d since B_{max} in the *VRI* bands and these are listed in Table 6. We find that the late-time decay rates of SN 2014dt in the *V* band are steeper than the standard $^{56}\mathrm{Co} \rightarrow {}^{56}\mathrm{Fe}$ (0.0098 mag d^{-1}) decay rates, indicating efficient gamma-ray and/or positron trapping. For comparison, we also list the very late time (230–380 d) decay rates of SN 2005hk in Table 6. The behaviour of the late-time light curve is an important tool to understand the magnetic field structure (Colgate, Petschek & Kriese 1980; Ruiz-Lapuente & Spruit 1998; Milne, The & Leising 1999, 2001). The configuration of the magnetic field is associated with the fraction of deposited positron energy. The flattening seen in the late-time light curve indicates trapping of a significant fraction of positrons, which implies a strong and tangled magnetic field instead of a weak magnetic field configuration (Stritzinger & Sollerman 2007).

We estimate the peak absolute magnitude of SN 2014dt to be $M_V = -18.33 \pm 0.02$ mag. Based on the estimate of peak brightness, SN 2014dt is similar to SN 2005hk ($M_V = -18.08 \pm 0.29$ mag; Phillips et al. 2007) and SN 2012Z ($M_V = -18.50 \pm 0.09$ mag; Stritzinger et al. 2015). For SN 2014dt, Foley et al. (2016) estimate the peak absolute magnitude $M_V = -17.4 \pm 0.5$ mag. This difference in peak absolute magnitude arises because of the different distances adopted by Foley et al. (2015) and this work.

5.2 Evolution of colours

The $B - V$, $V - I$, $V - R$ and $R - I$ colour curves of SN 2014dt are shown in Fig. 3 and compared with four other Type Iax SNe (see Table 7). The colour curves of all SNe are corrected for reddening values given in Table 7. From Fig. 3, we see that for most Type Iax SNe, the colour evolution is studied up to a time-span of less than 100 d whereas in the case of SN 2014dt we have estimates of colours from 30 to 200 d. Between 30 and 70 d, the $B - V$ colours of SN 2014dt closely resemble the colour evolution of SN 2005hk with slightly bluer colours. The $B - V$ colour evolution of SN 2014dt follows a bluer trend up to ∼170 d. The $V - I$, $V - R$ and $R - I$ evolutions are nearly constant up to ∼100 d and are redder at later phases. At phase ∼70 d, the $V - I$, $V - R$ and $R - I$ colour evolutions are similar to SN 2005hk. We notice some dip-like features in $V - R$ and $R - I$ colours close to +200 d possibly resulting from a scatter in the *V*-, *R*- and *I*-band data.
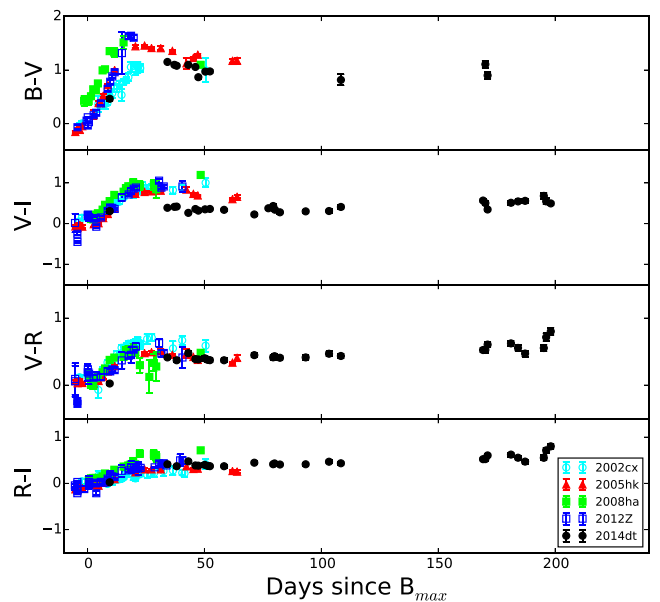

Figure 3. The comparison of $B - V$, $V - I$, $V - R$ and $R - I$ colour evolutions of SN 2014dt with four other Type Iax SNe. The error bars are smaller than the point size.

5.3 Bolometric light curve

The light curves of Type Ia SNe are powered by the radioactive decay of $^{56}\mathrm{Ni} \rightarrow {}^{56}\mathrm{Co} \rightarrow {}^{56}\mathrm{Fe}$ and the peak luminosity is directly related to the amount of $^{56}\mathrm{Ni}$ synthesized in the explosion (Arnett 1982). The Arnett formulation is applied to the bolometric light curve for estimating various physical parameters such as $^{56}\mathrm{Ni}$ mass, ejected mass M_{ej} and kinetic energy E_{k} of the explosion. The underlying assumptions of the Arnett model are homologous expansion of ejecta, dominance of radiation pressure, constant opacity, distribution of $^{56}\mathrm{Ni}$ peaking towards the ejected mass centre, small initial radius of explosion, etc. (Arnett 1982). Most of the flux at early times emerges in the optical wavelength for a Type Ia SN and hence the quasi-bolometric luminosity obtained using optical bands gives a good estimate of the total bolometric luminosity (*UVOIR*). We construct the quasi-bolometric light curve of SN 2014dt by

Table 7. Properties of the comparison sample. The references are: 1, Li et al. (2003), NED; 2, Sahu et al. (2008) and Phillips et al. (2007), NED; 3, Foley et al. (2009); 4, Stritzinger et al. (2014); 5, Stritzinger et al. (2015) and Yamanaka et al. (2015); 6, Tomasella et al. (2016), NED.

SNe	Distance (Mpc)	Extinction $E(B-V)$ (mag)	M_B (mag)	M_V (mag)	Δm_{15} (mag)	Reference
SN 2002cx	102.7 ± 7.2	0.034	-17.68 ± 0.10	-17.57 ± 0.15	1.29 ± 0.11	1
SN 2005hk	48.6 ± 3.4	0.110	-18.02 ± 0.32	-18.08 ± 0.29	1.68 ± 0.05	2
SN 2008ha	21.3	0.081	-13.74 ± 0.15	-14.21 ± 0.15	2.17 ± 0.02	3
SN 2010ae[a]	13.1 ± 3.5	0.600	-13.44 ± 0.54	-13.80 ± 0.54	2.43 ± 0.11	4
SN 2012Z[b]	29.8 ± 3.8	$0.036/0.11 \pm 0.03$	-18.27 ± 0.09	-18.50 ± 0.09	1.43 ± 0.02	5
SN 2014ck	24.4 ± 1.7	0.500	-17.37 ± 0.15	-17.29 ± 0.15	1.76 ± 0.15	6

Notes. [a] A range of M_B and M_V is given for SN 2010ae in Stritzinger et al. (2014); we have mentioned the lower value in this paper.
[b] Two different total extinction values were adopted by Yamanaka et al. (2015) and Stritzinger et al. (2015). For constructing the bolometric light curve and colour curve of SN 2012Z, we have used the extinction value adopted by Stritzinger et al. (2015) and data files were taken from Yamanaka et al. (2015).
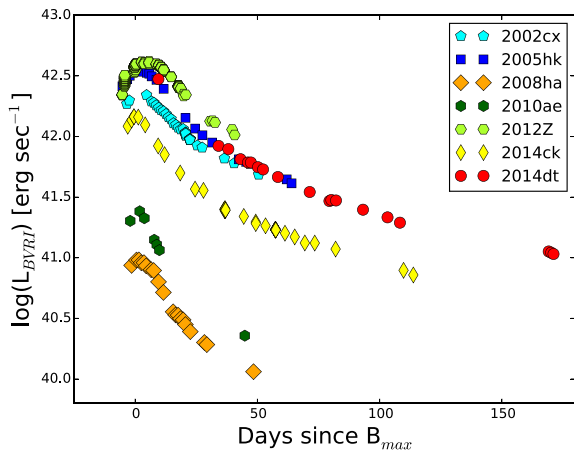
Figure 4. *BVRI* quasi-bolometric light curve of SN 2014dt. A comparison with *BVRI* quasi-bolometric light curves of other Type Iax SNe – SN 2002cx (Li et al. 2003), SN 2005hk (Sahu et al. 2008), SN 2008ha (Foley et al. 2009), SN 2010ae (Stritzinger et al. 2014), SN 2012Z (Stritzinger et al. 2015; Yamanaka et al. 2015) and SN 2014ck (Tomasella et al. 2016) – shows that the luminosity of SN 2014dt is similar to SN 2005hk.

converting the extinction-corrected *BVRI* magnitudes to fluxes by using zero-points from Bessell, Castelli & Plez (1998). The total flux in the *BVRI* bands is estimated by integrating the flux between *B* and *I* bands using a trapezoidal rule and converted to luminosity by using the luminosity distance (assuming $H_0 = 73 \pm 5$ km s^{-1} Mpc^{-1}, $\Omega_m = 0.27$ and $\Omega_v = 0.73$). The quasi-bolometric light curves of the SNe in our sample – SN 2002cx (Li et al. 2003), SN 2005hk (Sahu et al. 2008), SN 2008ha (Foley et al. 2009), SN 2010ae (Stritzinger et al. 2014), SN 2012Z (Stritzinger et al. 2015; Yamanaka et al. 2015) and SN 2014ck (Tomasella et al. 2016) – are constructed in the same manner as discussed above for SN 2014dt. The quasi-bolometric light curve of SN 2014dt is shown in Fig. 4 along with a sample of Type Iax SNe. From the figure, it is clear that the luminosity of SN 2014dt is comparable to SN 2005hk.

However, the true bolometric luminosity results from the contribution of *UV*, optical and IR bands. In the case of SN 2014dt, we only have the optical bands and hence we are missing contributions from the *UV* and IR bands. Because these peculiar events are rare, it is difficult to apply a well-defined correction for the

missing bands, which can be easily done in the case of Type Ia SNe (Suntzeff 1996; Contardo, Leibundgut & Vacca 2000). Both SNe 2005hk and 2012Z have *U* and IR observations, which can be used to estimate the contribution of *U* and IR bands to the optical (*BVRI*) luminosity. We find that the total contribution of *U* and IR bands is between 20 and 30 per cent at peak. Tomasella et al. (2016) also find that the *U* and IR bands contribute ∼35 per cent at peak in SN 2014ck. We apply the Arnett model to the quasi-bolometric light curve of SN 2005hk (assuming constant optical opacity $k_{opt} = 0.1$ cm^2 g^{-1} and constant of integration $\beta = 13.6$) and we estimate the ^{56}Ni mass to be 0.14 M$_\odot$, ejecta mass $M_{ej} = 0.98$ M$_\odot$ and kinetic energy $E_k = 0.41 \times 10^{51}$ erg for a photospheric velocity of 6500 km s^{-1}. After correcting for the missing *U* and IR bands flux (as discussed above) of SN 2005hk, we estimate the ^{56}Ni mass to be 0.19 M$_\odot$. The results of the Arnett model are in good agreement with those found in Sahu et al. (2008), Phillips et al. (2007) and Stritzinger et al. (2015) for SN 2005hk. The ejecta masses of SN 2005hk that are estimated by Sahu et al. (2008, Chandrasekhar mass ejecta, photospheric velocity 6500–6000 km s^{-1} at -6 and $+3$ d respectively), Stritzinger et al. (2015, ejecta mass between 1.5 and 2.0 M$_\odot$, photospheric velocity between 5000 and 7000 km s^{-1}) and this work vary because of the values of the photospheric velocity used in the calculation and the different methods used. We have taken the upper limit, keeping in view the remarkable similarities between SN 2005hk and SN 2014dt, and we can say that a comparable amount of ^{56}Ni would have been ejected in the explosion of SN 2014dt. Using the analytical expressions in Maeda et al. (2003) and Yamanaka et al. (2015), we fit a late-phase energy deposition function to the nebular phase bolometric light curve of SN 2014dt and we estimate the ejecta mass to be 0.95 M$_\odot$, which is in agreement with the values obtained using the Arnett model at early times.

6 SPECTRAL EVOLUTION

We present spectral evolution at 18 epochs between 23 and 157 d after B_{max} in Figs 5, 6 and 7. Telluric features have not been removed from the spectra and are marked in Fig. 5. Line identification has been done following Branch et al. (2004). We run the SNID (Blondin & Tonry 2007) spectral identification code on our early-phase spectrum, which corresponds to 23 d since B_{max}. The earliest spectrum at 23 d (Fig. 5) is dominated by Fe II and Co II lines. Features due to the Cr II (∼4800 Å) and Na ID (5890 Å)
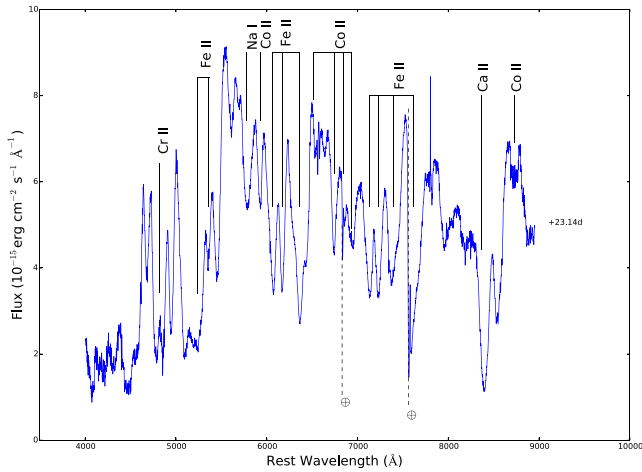
Figure 5. The earliest spectrum of SN 2014dt at 23 d is shown. The phase is calculated with respect to B_{max}. Line identification is done using Branch et al. (2004). Telluric features are also shown.

lines are also present. In the red region, NIR features due to Ca II (NIR triplet) and Co II are also seen. The Si II line at ∼6150 Å is not seen in our first spectrum obtained at 23 d. This line is the identifying feature of Type Ia SNe during the early photospheric phase, which gradually disappears and becomes blended with other lines such as Fe, Co, etc. In Fig. 6, the spectral evolution during the period 29–98 d is presented. Around 42 d, the lines due to Co II in the wavelength range 6500–6800 Å evolve fast in compar-

ison to other lines. The spectral evolution between 105 and 157 d shows an increase in the emission lines (Fig. 7), as expected in a SN spectra when the ejecta becomes optically thin. The late phases mark the disappearance of Cr II lines around 4800 Å; however, new features due to Fe II multiplets (λ5000 Å) and O I (λ7773 Å) appear in the spectra. The blue continuum weakens as the spectra evolves.

Type Iax SNe form a distinct class and each SN shows some unique features. We have compared spectral evolution at different phases with other well-studied SN 2002cx (Li et al. 2003), SN 2005hk (Sahu et al. 2008), SN 2008ge (Foley et al. 2010a), SN 2012Z (Stritzinger et al. 2015) and SN 2015H (Magee et al. 2016).

The earliest spectrum (23 d) of SN 2014dt has a good match at different line-forming regions with all five SNe used for comparison (see the tope panel of Fig. 8). The two absorption dips due to Fe II lines at 7308 and 7462 Å are clearly seen in SNe 2012Z and 2014dt, with a slight hint in SN 2015H and a single absorption dip in SNe 2005hk and 2002cx (presented in the enlarged view in Fig. 8). Because we have not done telluric correction, this might be the region where telluric line 7603 Å also comes. SN 2014dt is clearly affected by telluric lines. The Co triplet at wavelength range 6500–6800 Å in SN 2014dt best matches with SN 2015H in comparison to other SNe (Fig. 8).

At 61 d, the overall spectrum of SN 2014dt is similar to other Type Iax SNe. The Fe II multiplet near 6000 Å of SN 2014dt matches well with other SNe such as SN 2002cx, SN 2005hk and SN 2015H, and only SN 2008ge has a poor resemblance with SN 2014dt in this wavelength regime. Co II features at 6521 and 6578 Å are clearly visible for SN 2002cx, two closely spaced peaks are seen for SN
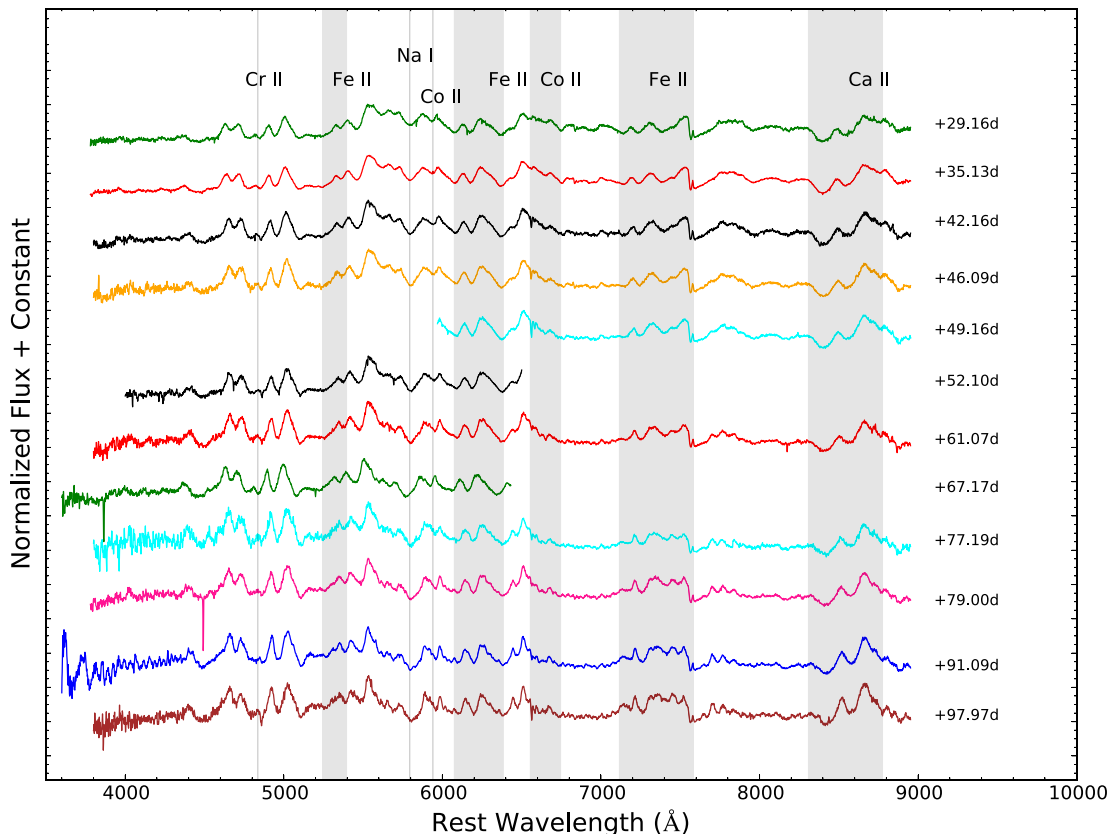

Figure 6. Spectral evolution of SN 2014dt during the period 29–98 d relative to B_{max}. Line identification is based on Branch et al. (2004). The different lines are indicated by shaded regions.
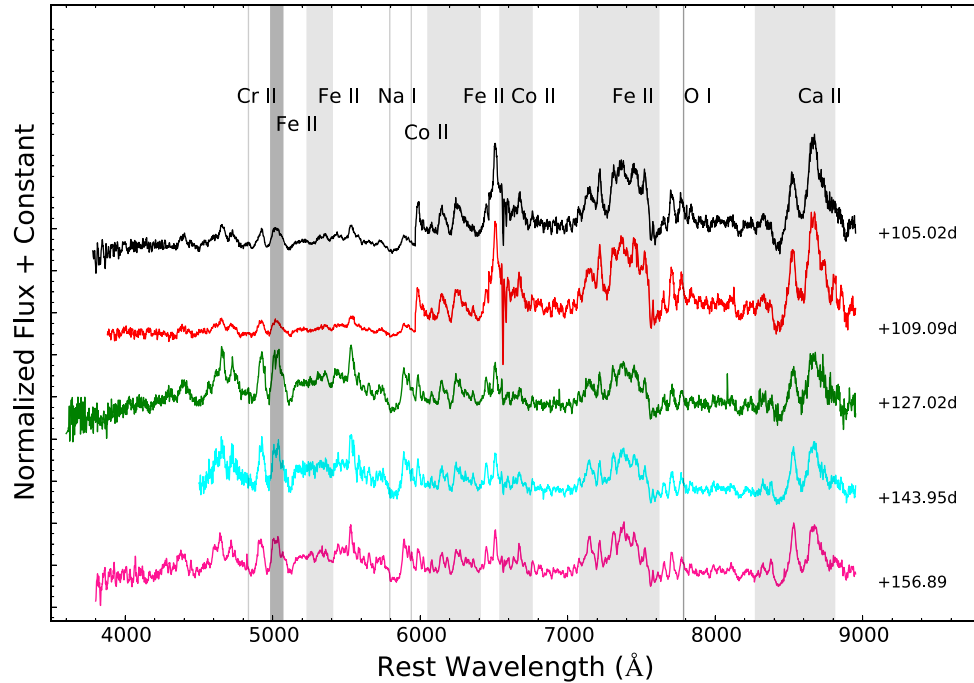
Figure 7. Spectral evolution of SN 2014dt from phase 105 d to 157 d relative to B_{max}. Line identification is based on Branch et al. (2004). The different lines are indicated by shaded regions.

2005hk and a single absorption peak is seen for SNe 2008ge and 2015H, whereas in SN 2014dt the emission lines are marginally double-peaked. The comparison plot along with the zoomed view of differences is shown in Fig. 8 (bottom panel).

The late-time spectrum (157 d) of SN 2014dt is compared with SNe 2008ge and 2012Z in Fig. 9. The overall spectral features of SN 2008ge are similar to SN 2014dt except for the feature at ~7300 Å (identified as [Fe II]), which increases in strength with time (Foley et al. 2010a). This broad emission feature is a result of blending of the [Fe II] line with other lines. In SN 2014dt, the blending is less than seen in SNe 2008ge and 2012Z. The region of interest, discussed above, is marked with a dark shaded region in Fig. 9. The NIR triplet is also present in SNe 2014dt, 2008ge and 2012Z along with different blending factors as discussed above. All the lines in SN 2014dt are narrower than SNe 2008ge and 2012Z.

6.1 Velocity evolution

We estimate the velocities of a few lines, Fe II 6149 Å, Fe II 6247 Å, Fe II 7449 Å, Fe II 7690 Å and Ca II 8662 Å by measuring the absorption minima (Fig. 10). Spectral evolution of SN 2014dt is enriched with Fe II lines and their evolution is significantly prominent. All the estimated line velocities are nearly half of the velocities usually found in typical Type Ia SNe. For SN 2014dt, the Fe II 7449 Å line shows a linear decline (velocity falls from 1700 to 1100 km s^{-1}) up to ~50 d and other lines such as Fe II 6149 Å, Fe II 6247 Å, Fe II 7690 Å and Ca II 8662 Å show a linear decline followed by a nearly constant evolution. Velocity gradient for all the lines are very small during the entire spectral sequence. In Fig. 10, we also show the velocity evolution measured from Fe II 6149 Å for SNe 2002cx, 2005hk and 2015H (Magee et al. 2016) and SN 2014ck (Tomasella

et al. 2016). At the phase of SN 2014dt beyond 20 d, SNe 2002cx and 2005hk both show higher velocity than SN 2014dt, whereas SNe 2014ck and 2015H are both associated with lower velocities compared to SN 2014dt. Velocities associated with SNe 2002cx and 2005hk are nearly 500 km s^{-1} higher than velocities associated with SN 2014dt. SNe 2014ck and 2015H are associated with velocities nearly 2500 and 500 km s^{-1}, respectively, lower than velocities associated with SN 2014dt. The estimated velocities of different lines are indicative of the fact that the explosion energy associated with SN 2014dt is low (0.24×10^{51} erg for a photospheric velocity of 5000 km s^{-1} and ejecta mass 0.98 M$_\odot$) compared to normal Type Ia SNe (1.39×10^{51} erg; Willcox et al. 2016). If we consider a M_{ch} white dwarf, then for a photospheric velocity of 5000 km s^{-1} the kinetic energy is 0.35×10^{51} erg, which is higher than that obtained for SN 2014dt.

6.2 Spectral modelling

We have used parametrized spectrum synthesis code SYN++ (Branch et al. 2007; Thomas, Nugent & Meza 2011) for spectral modelling. We model the first four epochs (23, 29, 35 and 42 d since B_{max}) of SN 2014dt with spectral synthesis code SYN++. In Fig. 11, we present the observed spectra with the output synthetic spectra generated by the SYN++ code. It was not possible to fit some of the broad emission features due to the local thermodynamic equilibrium approximation and resonance scattering of this code. Fe II and Co II features match very well. The Fe [III] doublet at the 4700 Å Co II and Fe II lines is fitted well. Co II and Fe II lines between 6700 and 7700 Å are also well produced. Although the NIR region is difficult to reproduce, the dip due to Ca is visible in the modelled spectra. As the phase increases, absorption profiles become sharper and deeper with the photospheric velocities gradually decreasing from 4500 to 3800 km s^{-1}. For fitting all the later phases, we use
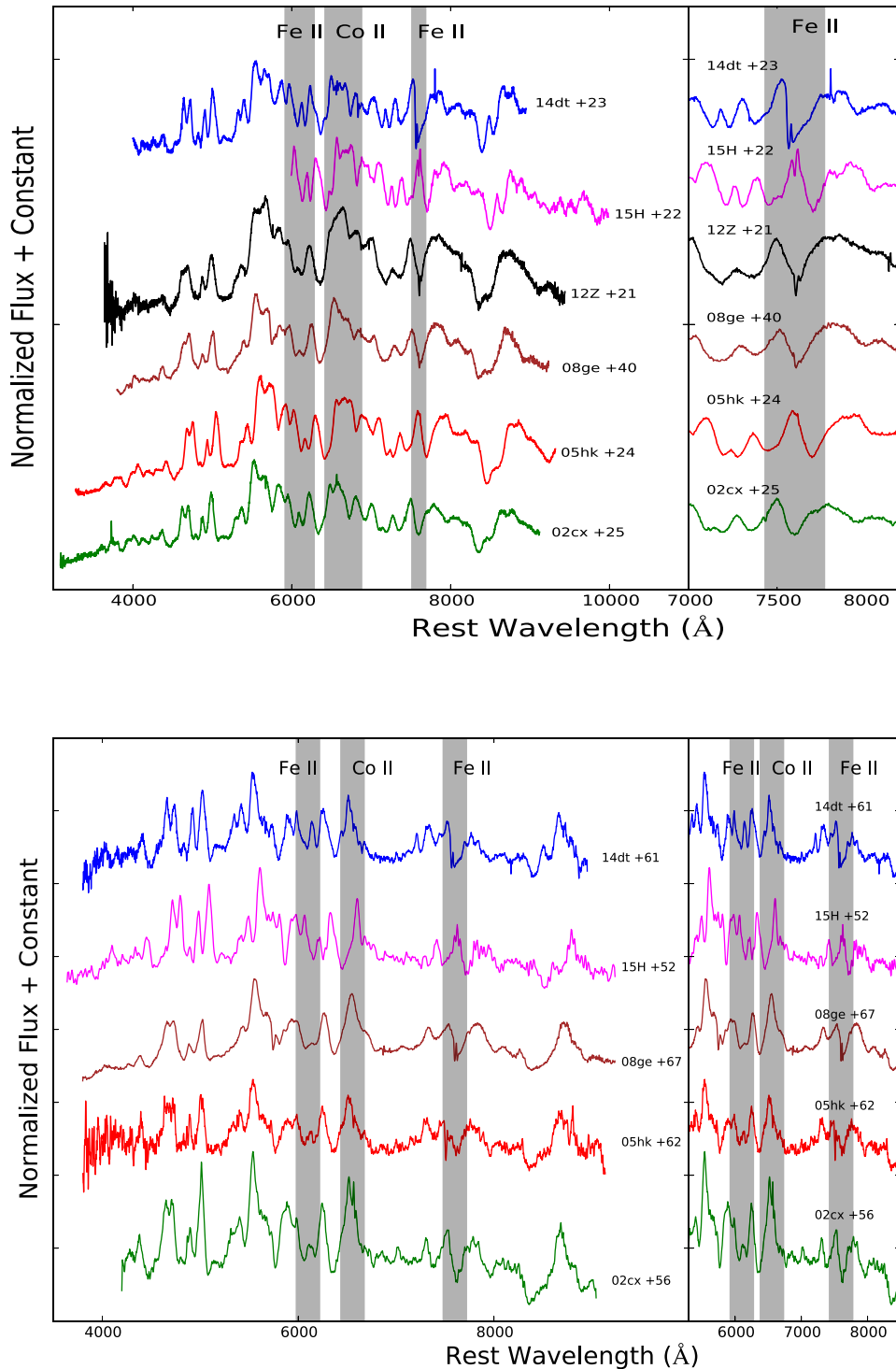
Figure 8. A comparison of SN 2014dt spectra at different epochs with other well-studied Type Iax SNe. All spectra have been shifted on a relative scale and shifted vertically for clarity. Top: a comparison of SN 2014dt at phase 23 d is shown. Bottom: at 61 d, there is overall a similarity between all the SNe except for some line-forming regions shown by the dark shade. Also, demarcating features are presented in an enlarged view. A full description of the observed features has been given in the text.

the same species and parameters (as used in the 23-d spectrum) with gradual changes, which indicates the slow evolution of ejecta configurations. The Boltzmann excitation temperature varies between 7000 and 4400 K for different lines. Also, the range for blackbody temperature was 8000–6600 K.

7 SUMMARY

SN 2014dt belongs to the subclass of Type Iax SNe and resembles other Type Iax SNe. Because SN 2014dt was discovered post-peak, the template fitting method yields a best match to the light curves of SN 2005hk with an estimated peak magnitude of 13.59 ± 0.04 mag
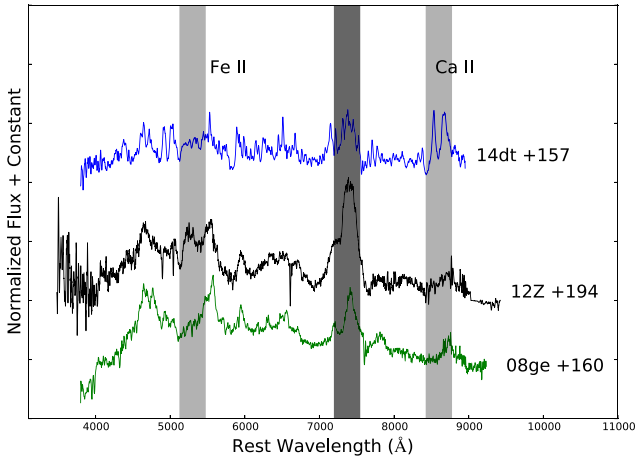
Figure 9. Comparison of the late nebular phase spectrum of SN 2014dt with SNe 2008ge and 2012Z. The most noticeable features around 7300 and 7400 Å are shown by a relatively dark shade. For SNe 2008ge and 2012Z, there are broad emission features with blending of a considerable number of ions. For SN 2014dt, there is no prominent blending so line identification is easy. The Fe II multiplet at 5200 and 5400 Å along with the NIR triplet are present in all three SNe 2014dt, 2012Z and 2008ge.
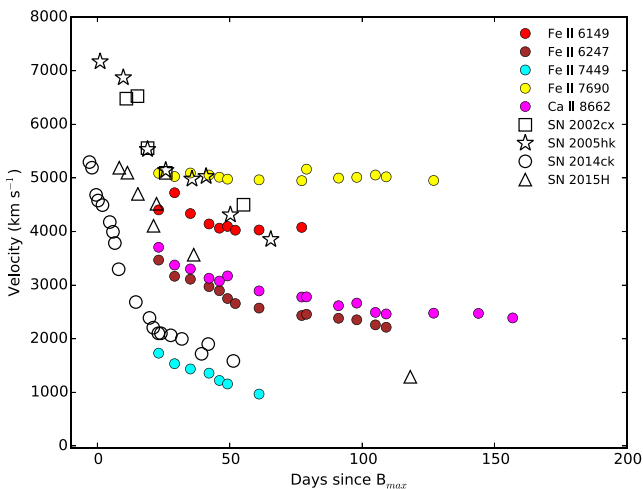
Figure 10. Absorption minima evolution of a few lines for SN 2014dt and its comparison with SNe 2002cx, 2005hk, 2014ck and 2015H.

in the B band and the epoch of maximum JD $= 245\,6950.34$. Late-phase light curves of SN 2014dt show some flattening, which is explained by gamma-ray and/or positron trapping. The $B - V$ colour of SN 2014dt is marginally bluer than SN 2005hk, but the overall colour evolution of SN 2014dt is similar to SN 2005hk.

On the basis of the estimated peak absolute magnitude ($M_V = -18.33 \pm 0.02$ mag), we can conclusively say that SN 2014dt falls in the category of bright Type Iax SNe such as SN 2005hk and SN 2012Z. The same can be inferred from Fig. 12, which is a scatter plot of absolute magnitude in the B band (M_B) and $\Delta m_{15}(B)$ of a number of Type Iax SNe and a sample of Type Ia SNe. The photometric properties of SN 2014dt are strikingly similar to those of SN 2005hk, and hence we can say that the explosion parameters of SN 2014dt will be comparable to those of SN 2005hk. For SN 2005hk, we estimate ^{56}Ni between 0.14 and 0.19 M$_\odot$ using the Arnett method with ejecta mass $M_{\rm ej} = 0.98$ M$_\odot$ and kinetic energy of explosion $E_k = 0.41 \times 10^{51}$ erg. We suggest

that the amount of synthesized ^{56}Ni in the explosion of SN 2014dt would be at least 0.14 M$_\odot$. Using a late-phase energy deposition function in the nebular phase bolometric light curve of SN 2014dt, we find the ejecta mass to be 0.95 M$_\odot$. Low explosion energy and low ^{56}Ni mass associated with SN 2014dt make it less luminous compared to Type Ia SNe.

Our spectroscopic campaign started 23 d since $B_{\rm max}$. Spectroscopic features of SN 2014dt have fairly good resemblance with other Type Iax SNe. The observed spectra are modelled with lower blackbody temperature (8000–6600 K) and lower photospheric velocities (4500–3800 km s^{-1}). The velocity evolution feature also confirms the low-energy budget of SN 2014dt, a typical feature of peculiar Type Iax SNe. The velocity of absorption minima for a number of lines varies between $\sim$1500 and $\sim$5500 km s^{-1}.

SN 2014dt has pre-explosion *HST* images and is second deepest after SN 2012Z. With pre-explosion images of SN 2014dt, Foley et al. (2015) did not detect any stellar source at the SN location to relatively deep limits and they concluded that the progenitor system of SN 2014dt was less luminous in the B band than SN 2012Z. The plausible progenitor of SN 2014dt could be a carbon oxygen white dwarf primary/helium-star companion, similar to SN 2012Z with a slightly smaller or hotter donor (Foley et al. 2015). The IR excess seen in the late-time light curves implies the association of the progenitor with a pre-existing dust shell, which includes a binary system with a red giant, a red supergiant or an asymptotic giant branch star as a mass donor (Fox et al. 2016). Foley et al. (2016) claimed on the basis of their existing data that the observed IR excess cannot be accounted for by dust emission; instead, the plausible reason for strong IR flux seen about 315 d after maximum brightness is from a bound remnant with an extended optically thick super-Eddington wind. The bound remnant mechanism is consistent with the late-time data of Type Iax SNe and could also be valid for SN 2014dt.

Continued late-time observations of SN 2014dt will be necessary to put constraints on the progenitor system and to conclude if the emission is dominated by the bound remnant. In many cases, the chances of late-time detection are hampered by the object's distance, its faintness or its location close to a bright host galaxy nucleus. The proximity of SN 2014dt and its location in the host galaxy is ideal for a late-time detection and this makes the object an excellent candidate for long-term monitoring.
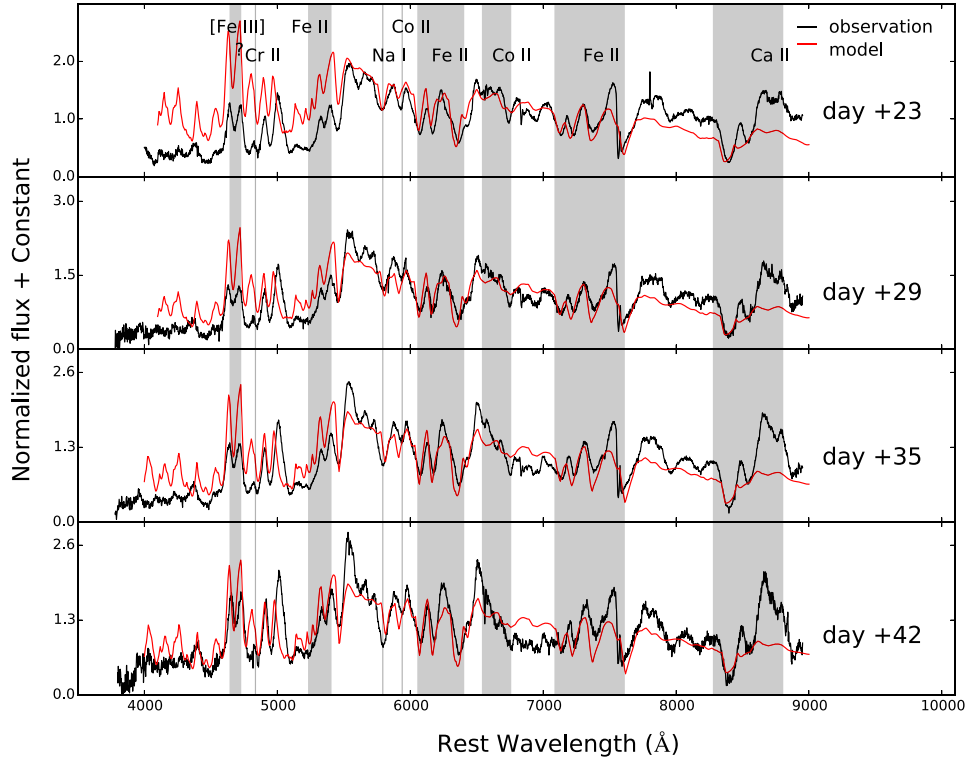
Figure 11. A comparison between early-phase observed spectra of SN 2014dt and synthetic spectra generated by the SYN++ code. Prominent absorption features are marked with the shaded region.
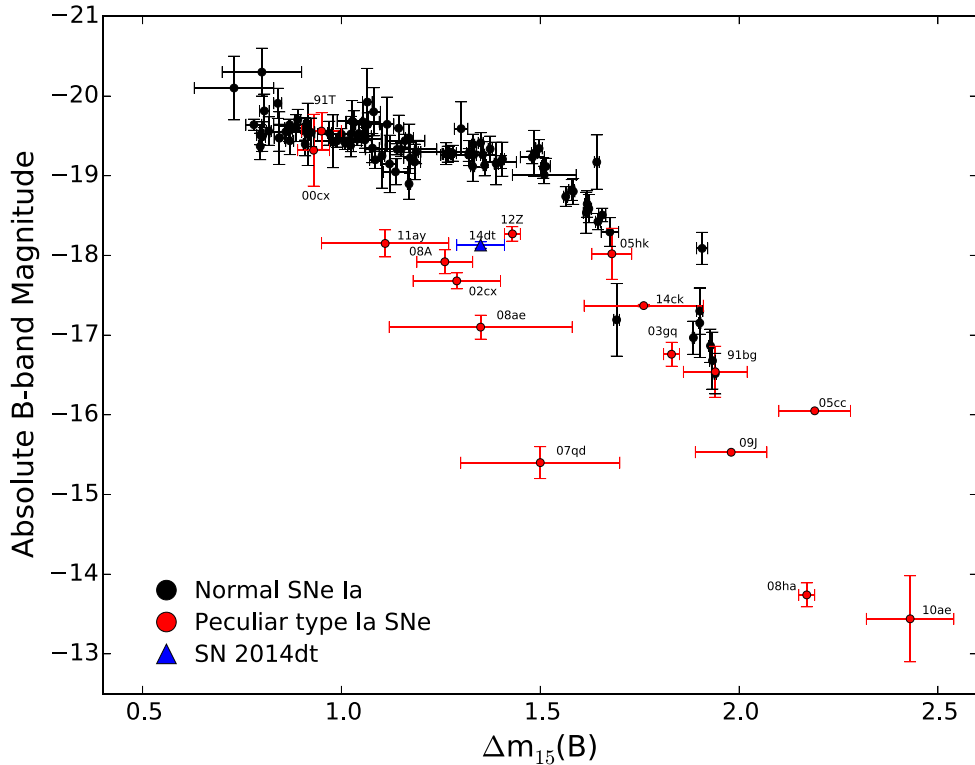

Figure 12. Absolute *B*-band magnitude versus decline rate Δm_{15} for a sample of Type Iax SNe: SN 1991T (Gibson & Stetson 2001), SN 1991bg (Turatto et al. 1996), SN 2000cx (Li et al. 2001), SN 2002cx (Li et al. 2003), SN 2003gq (Foley et al. 2013), SN 2005cc (Foley et al. 2013, our computed value), SN 2005hk (Sahu et al. 2008), SN 2007qd (McClelland et al. 2010), SN 2008A (Foley et al. 2013), SN 2008ae (Foley et al. 2013), SN 2008ha (Foley et al. 2009), SN 2010ae (Stritzinger et al. 2014), SN 2011ay (Szalai et al. 2015), SN 2012Z (Stritzinger et al. 2015), SN 2014ck (Tomasella et al. 2016) and SN 2014dt (this work). Normal Type Ia SNe (Jha et al. 2006; Jha, Riess & Kirshner 2007; Ganeshalingam et al. 2010; Stritzinger et al. 2015) are also shown.

REFERENCES

Arnett W. D., 1982, ApJ, 253, 785

Bessell M. S., Castelli F., Plez B., 1998, A&A, 333, 231

Binggeli B., Sandage A., Tammann G. A., 1985, AJ, 90, 1681

Blondin S., Tonry J. L., 2007, ApJ, 666, 1024

Bose S., Kumar B., 2014, ApJ, 782, 98

Bottinelli L., Gouguenheim L., Paturel G., de Vaucouleurs G., 1984, A&AS, 56, 381

Branch D., Baron E., Thomas R. C., Kasen D., Li W., Filippenko A. V., 2004, PASP, 116, 903

Branch D., Parrent J., Troxel M. A., Casebeer D., Jeffery D. J., Baron E., Ketchum W., Hall N., 2007, in di Salvo T., Israel G. L., Piersant L., Burderi L., Matt G., Tornambe A., Menna M. T., eds, AIP Conf. Ser. Vol. 924, The Multicolored Landscape of Compact Objects and Their Explosive Origins. American Institute of Physics, New York, p. 342

Colgate S. A., Petschek A. G., Kriese J. T., 1980, ApJ, 237, L81

Contardo G., Leibundgut B., Vacca W. D., 2000, A&A, 359, 876

Filippenko A. V., Foley R. J., Silverman J. M., Blondin S., Matheson T., Berlind P., 2007a, Central Bureau Electronic Telegrams, 817

Filippenko A. V., Foley R. J., Silverman J. M., Chornock R., Li W., Blondin S., Matheson T., 2007b, Central Bureau Electronic Telegrams, 926

Fink M. et al., 2014, MNRAS, 438, 1762

Foley R. J. et al., 2009, AJ, 138, 376

Foley R. J. et al., 2010a, AJ, 140, 1321

Foley R. J., Brown P. J., Rest A., Challis P. J., Kirshner R. P., Wood-Vasey W. M., 2010b, ApJ, 708, L61

Foley R. J. et al., 2013, ApJ, 767, 57

Foley R. J., Van Dyk S. D., Jha S. W., Clubb K. I., Filippenko A. V., Mauerhan J. C., Miller A. A., Smith N., 2015, ApJ, 798, L37

Foley R. J., Jha S. W., Pan Y-C., Zheng W. K., Bildsten L., Filippenko A. V., Kasen D., 2016, MNRAS, 461, 433

Fox O. D. et al., 2016, ApJ, 816, L13

Ganeshalingam M. et al., 2010, ApJS, 190, 418

Gibson B. K., Stetson P. B., 2001, ApJ, 547, L103

Jha S. et al., 2006, AJ, 131, 527

Jha S., Riess A. G., Kirshner R. P., 2007, ApJ, 659, 122

Jordan IV G. C., Perets H. B., Fisher R. T., van Rossum D. R., 2012, ApJ, 761, L23

Kromer M. et al., 2013, MNRAS, 429, 2287

Kromer M. et al., 2015, MNRAS, 450, 3045

Landolt A. U., 2009, AJ, 137, 4186

Lee N., Li W., Newton J., Puckett T., 2007, Central Bureau Electronic Telegrams, 809

Li W. et al., 2001, PASP, 113, 1178

Li W. et al., 2003, PASP, 115, 453

Liu Z-W., Moriya T. J., Stancliffe R. J., Wang B., 2015a, A&A, 574, A12

Liu Z-W., Stancliffe R. J., Abate C., Wang B., 2015b, ApJ, 808, 138

McClelland C. M. et al., 2010, ApJ, 720, 704

McCully C. et al., 2014a, Nature, 512, 54

McCully C. et al., 2014b, ApJ, 786, 134

Maeda K., Mazzali P. A., Deng J., Nomoto K., Yoshii Y., Tomita H., Kobayashi Y., 2003, ApJ, 593, 931

Magee M. R. et al., 2016, A&A, 589, A89

Milne P. A., The L-S., Leising M. D., 1999, ApJS, 124, 503

Milne P. A., The L-S., Leising M. D., 2001, ApJ, 559, 1019

Moriya T., Tominaga N., Tanaka M., Nomoto K., Sauer D. N., Mazzali P. A., Maeda K., Suzuki T., 2010, ApJ, 719, 1445

Nakano S. et al., 2014, Central Bureau Electronic Telegrams, 4011

Narayan G. et al., 2011, ApJ, 731, L11

Ochner P., Tomasella L., Benetti S., Cappellaro E., Elias-Rosa N., Pastorello A., Turatto M., 2014, Central Bureau Electronic Telegrams, 4011

Pejcha O., Prieto J. L., 2015, ApJ, 799, 215

Phillips M. M. et al., 2007, PASP, 119, 360

Prabhu T. P., Anupama G. C., 2010, in Ojha D. K., ed., ASI Conf Ser. Vol. 1, Interstellar Matter and Star Formation: A Multi-wavelength Perspective. Astronomical Society of India, Bangalore, p. 193

Rajala A. M. et al., 2005, PASP, 117, 132

Rodríguez Ó., Clocchiatti A., Hamuy M., 2014, AJ, 148, 107

Roy R. et al., 2011, ApJ, 736, 76

Ruiz-Lapuente P., Spruit H. C., 1998, ApJ, 500, 360

Sagar R., 1999, Current Science, 77, 643

Sagar R., Kumar B., Omar A., Pandey A. K., 2012, in Stepp L. M., Gilmozzi R., Hall H. J., eds, Proc. SPIE 8444, Ground-based and Airborne Telescopes IV. SPIE, Bellingham, p. 84441T

Sahu D. K. et al., 2008, ApJ, 680, 580

Schlafly E. F., Finkbeiner D. P., 2011, ApJ, 737, 103

Schoeniger F., Sofue Y., 1997, A&A, 323, 14

Sparks W. B., 1994, ApJ, 433, 19

Stalin C. S., Hegde M., Sahu D. K., Parihar P. S., Anupama G. C., Bhatt B. C., Prabhu T. P., 2008, Bulletin of the Astronomical Society of India, 36, 111

Stetson P. B., 1987, PASP, 99, 191

Stetson P. B., 1992, JRASC, 86, 71

Stritzinger M., Sollerman J., 2007, A&A, 470, L1

Stritzinger M. D. et al., 2014, A&A, 561, A146

Stritzinger M. D. et al., 2015, A&A, 573, A2

Suntzeff N. B., 1996, in McCray R., Wang Z., eds, Supernovae and Supernova Remnants. Cambridge University Press, Cambridge, p. 41

Szalai T. et al., 2015, MNRAS, 453, 2103

Thomas R. C., Nugent P. E., Meza J. C., 2011, PASP, 123, 237

Tomasella L. et al., 2016, MNRAS, 459, 1018

Turatto M., Benetti S., Cappellaro E., Danziger I. J., Della Valle M., Gouiffes C., Mazzali P. A., Patat F., 1996, MNRAS, 283, 1

Valenti S. et al., 2009, Nature, 459, 674

van Dokkum P. G., 2001, PASP, 113, 1420

White C. J. et al., 2015, ApJ, 799, 52

Willcox D. E., Townsley D. M., Calder A. C., Denissenkov P. A., Herwig F., 2016, ApJ, 832, 13

Yamanaka M. et al., 2015, ApJ, 806, 191

Yaron O., Gal-Yam A., 2012, PASP, 124, 668

This paper has been typeset from a TEX/LATEX file prepared by the author.